INT. J. REMOTE SENSING, 1998, VOL. 19, NO. 16, 3055–3074

Passive microwave observations of inundation area and the area/stage relation in the Amazon River floodplain

S. J. SIPPEL†, S. K. HAMILTON‡, J. M. MELACK§ and E. M. M. NOVO¶

†Institute for Computational Earth System Science (ICESS), University of California, Santa Barbara, California 93106–3060, USA. Correspondence to: Kellogg Biological Station, Michigan State University, 3700 E. Gull Lake Drive, Hickory Corners, Michigan 49060–9516, USA; email: sippel@kbs.msu.edu

‡Kellogg Biological Station, Michigan State University, 3700 E. Gull Lake Drive, Hickory Corners, Michigan 49060–9516, USA

§School of Environmental Science and Management, and ICESS, University of California, Santa Barbara, California 93106–3060, USA

¶Divisão de Sensoriamento Remoto, Instituto Nacional de Pesquisas Espaciais, Caixa Postal 515, CEP 12201, São José dos Campos, SP, Brazil

(*Received 3 March 1997; in final form 14 January 1998*)

Abstract. Inundation patterns in Amazon River floodplains are revealed by analysis of the 37 GHz polarization difference observed by the Scanning Multichannel Microwave Radiometer on the Nimbus-7 satellite. Flooded area is estimated at monthly intervals for January 1979 through August 1987 using mixing models that account for the major landscape units with distinctive microwave emission characteristics. Results are presented separately for 12 longitudinal reaches along the Amazon River main stem in Brazil as well as for three major tributaries (the Jurua, Purus and Madeira rivers). The total area along the Amazon River main stem that was flooded (including both floodplain and open water) varied between 19 000 and 91 000 km^2. The correlation between flooded area and river stage is used to develop a predictive relationship and reconstruct regional inundation patterns in the floodplain of the Amazon River main stem over the past 94 years of stage records (1903–1996). The mean flooded area along the Amazon River during this 94-year period was 46 800 km^2, of which the open-water surfaces of river channels and floodplain lakes comprised about 20 700 km^2.

1. Introduction

The Amazon River and its tributaries seasonally overflow their banks to inundate extensive floodplains, and information on the inundation patterns in these floodplains is needed for a variety of purposes. The ecological characteristics of these floodplain ecosystems—including the productivity of riverine fisheries—are largely determined by the spatial and temporal variation of seasonal inundation (Junk 1997). Where the floodplains are inhabited by humans or utilized for agriculture, information on inundation patterns is useful for land-use planning and for the prediction of floods, which help local inhabitants adapt to the natural flood cycles of large rivers (Frechione *et al.* 1989). Assessment of the environmental impact of large-scale river development projects, such as construction of impoundments or navigation channels, requires comprehension of the hydrological linkages between the river channel and its adjacent floodplains (Petts 1990, Ligon *et al.* 1995).

Information on inundation patterns is also necessary to understand and model the hydrological and biogeochemical fluxes through the fluvial system, because fluvial transport can be altered by evaporative water losses, sediment retention, and nutrient transformations during temporary residence of river water on floodplains (Lewis and Saunders 1989, Richey *et al.* 1989 a, 1991, Mertes *et al.* 1996, Hamilton *et al.* 1997). An improved understanding of the fluvial export of water and materials from the Amazon Basin can illuminate biogeochemical cycles within the drainage basin as well as reveal controls on nutrient supply from the continents to the ocean, since the Amazon River is responsible for nearly 20% of the world's runoff to the oceans (Vörösmarty *et al.* 1989). Knowledge of the spatial and temporal variation in the area inundated on the floodplain is essential for the estimation of methane emission from the inundated floodplain environments to the atmosphere (Devol *et al.* 1990), which is an important part of the global methane budget because tropical wetlands are one of the world's largest natural sources of this greenhouse gas (Bartlett and Harriss 1993).

Despite the need to understand the hydrology of the river–floodplain system in the Amazon, information on flooding patterns in the basin has been difficult to acquire because of the vast and remote nature of the territory. Side-looking airborne radar images from the Brazilian Radambrasil project indicate the extent of the geomorphological floodplain, which likely represents the upper limit of the area that could be subject to riverine flooding at high water (Sippel *et al.* 1992). Variation in depth of water on the floodplain can be inferred from water level (stage) measurements made at a few stations along the main river channels, if detailed knowledge of the floodplain geomorphology is available (Mertes *et al.* 1996). Among the available options for remote sensing of spatial and temporal patterns in flooding, passive microwave observations from satellites offer regional-scale information of high temporal resolution. Optical remote sensing systems such as Landsat provide much better spatial resolution (e.g., 30 m for Landsat Thematic Mapper (TM)) but very limited temporal resolution in the Amazon Basin because of the frequent cloud cover and the difficulty of detecting flooding through vegetation canopies. Satellite-borne radar remote sensing potentially offers the combination of high spatial and temporal resolution of flooding patterns (Hess *et al.* 1995), but the necessary seasonal coverage over multiple years is not yet available.

Recent research using data from the 37 GHz channel of the Scanning Multichannel Microwave Radiometer (SMMR) has demonstrated the application of passive microwave remote sensing to study large tropical wetlands. Giddings and Choudhury (1989) showed that the major floodplains of South America could be delineated in images of the 37 GHz emission at horizontal and vertical polarizations. In a pilot study of the Amazon River floodplain near Manaus, Sippel *et al.* (1994) estimated flooded area using linear mixing models of the microwave emission from major landscape units. Hamilton *et al.* (1996) employed a similar approach to reveal inundation patterns throughout the Pantanal wetland, a vast savanna floodplain to the south of the Amazon Basin. Vörösmarty *et al.* (1996) investigated the potential of SMMR observations as an indicator of discharge in the Amazon River.

In this study we analyse the SMMR 37 GHz observations to estimate regional inundation patterns along the Amazon River main stem and three of its largest tributaries. We develop a predictive relation between river stage and flooded area along the Amazon River main stem that allows us to extend the inundation record from the 9-year SMMR observation period to a 94-year period (1903–1996). These data help to satisfy the aforementioned requirements for improved understanding of inundation patterns in these vast floodplain ecosystems.

2. SMMR passive microwave observations

The SMMR instrument measured the natural emission of microwave energy from the Earth's surface and atmosphere. Measurements are expressed as brightness temperatures (in Kelvins), and are available at several frequencies and at both vertical and horizontal polarizations (Fu *et al.* 1988). The difference between vertically and horizontally polarized brightness temperatures observed by satellite at the 37 GHz frequency (hereafter referred to as ΔT_{obs}) provides a sensitive indicator of the presence of surface water, particularly where water occurs against a background of vegetated land surfaces (Choudhury 1991). The theoretical basis for interpretation of 37 GHz emission has been reviewed by Choudhury (1989). The spatial resolution of the SMMR sensor is approximately 27 km at 37 GHz and the processed global data sets are gridded into cells of 0.25° latitude by longitude.

Satellite observations of 37 GHz emission are available for December 1978 to August 1987 from the SMMR instrument operated on board the Nimbus-7 satellite (Gloersen *et al.* 1984, Fu *et al.* 1988). Similar observations are available from the Special Sensor Microwave/Imager (SSM/I) instruments, which began operation in July 1987 and continue operation now as part of the Defense Meteorological Satellite Program (Hollinger *et al.* 1990). The algorithms developed in the present study for analysis of the SMMR observations cannot be directly applied to the SSM/I data because of differences in the sensor systems and data processing.

In this study, we use the SMMR observations for January 1979 to August 1987, which are drawn from the global data set of the 37 GHz ΔT_{obs} that was originally studied by Choudhury (1989, 1991). Global SMMR observations are available for approximately 6-day intervals, and are compiled separately for day and night (local equator crossings at noon and midnight). After calculation of ΔT_{obs} for each grid cell from the daytime brightness temperatures, the observations were ranked within each month and the second lowest value (usually out of four) was selected, thereby yielding one ΔT_{obs} value per month (Choudhury 1989). The screening served to eliminate outlying values that might have resulted from atmospheric scattering by heavy rainfall, or from temporary pooling of water on the land surface after heavy rainfalls. The May 1986 ΔT_{obs} values for all grid cells in our Amazon data set were inexplicably low and were therefore deleted from the time series.

3. Methods

3.1. *Delineation of study reaches*

The present study deals with the Brazilian portion of the Amazon River system. Within Brazil, the main stem of the Amazon River is called the Rio Solimões above the confluence with the Negro River and the Rio Amazonas below that confluence, although in this paper we collectively refer to the Solimões and Amazonas rivers as the Amazon River main stem. The fluvial systems of the Amazon Basin are described by Sioli (1984).

We divided the Amazon River main stem into 12 reaches bounded by 1° 30′ longitudinal divisions (figure 1). The reaches start at the western Brazilian border and extend downriver to just above the confluence with the Xingu River (Almeirim;

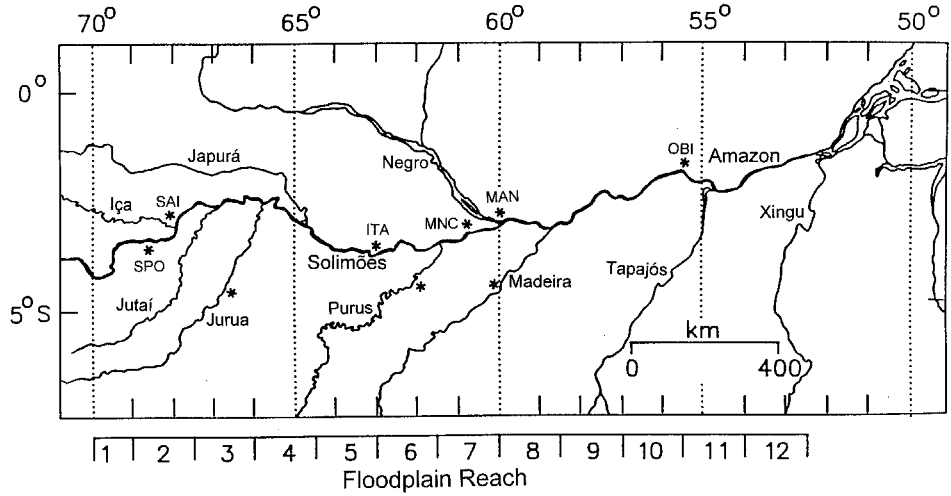

Figure 1. The Amazon River and its major tributaries. Flooded area was estimated for the 12 longitudinal reaches shown along the bottom of the map. Flooded area was also estimated for the Purus, Madeira and Jurua Rivers from 8° S (the southern border of this map) to their confluences with the Amazon River. River stage stations are marked by an asterisk; codes are as follows: SPO, São Paulo de Olivença; SAI, Santo Antônio de Içą; ITA, Itapeua; MNC, Manacapuru; MAN, Manaus; OBI, Óbidos. The Jurua River stage station is at Carauari, the Purus River station is at Beruri, and the Madeira River station is at Borba.

52° 30′ W). Upstream of the Brazilian border, the floodplain becomes increasingly narrow, and its effect on passive microwave emission becomes less distinguishable. We did not attempt to estimate inundation patterns downstream of reach 12 because of the increasing importance of short-term variation caused by tidal effects (Sioli 1966). Tidal effects are present in reaches 11 and 12 as well, but are on the order of 20 cm or less (E. Novo, unpublished data), and are thus unlikely to have a major effect on inundation area since the seasonal variation in river level in these reaches is *ca* 5 m. We also estimated inundation patterns along the lower reaches of three of the tributaries with the most extensive floodplains: the Purus, Jurua and Madeira rivers. Each of these tributaries was analysed as a single reach extending from near its mouth upstream to 8° S latitude (figure 1).

Within each reach, we aggregated 12–60 SMMR grid cells to enclose the river and its floodplain (table 1), and we calculated the mean ΔT_{obs} of the aggregate for each month. Aggregation reduces the relative uncertainty in location, since the geolocation error of the SMMR data may be as much as 12 km (Choudhury *et al.* 1992). The grid-cell aggregates encompassed the floodplain as it is delineated on 1:250 000 scale planimetric maps produced from Side-Looking Airborne Radar (SLAR) imagery by the Radambrasil project (Sippel *et al.* 1992). The proportion of upland area in the grid-cell aggregates (table 1) should be minimized because the upland dilutes the seasonal signal of the floodplain inundation, and can potentially contain wetland areas with flooding patterns that are distinct from the riverine floodplains. However, some upland was included along the edges of the aggregates to reduce the effect of geolocation error; for the floodplain of the Amazon River main stem we included at least one-half of a grid cell of upland surrounding the

Table 1. Characteristics of the grid-cell aggregates for each study reach. The table shows the number of grid cells in the aggregate, the open-water areas of the main-stem river channel and of permanent floodplain lakes, the fractional area of open water (f_w, which includes the river and lakes) and of uplands not subject to flooding, and the empirically determined values of ΔT_w and ΔT_f. Reaches 1–12 are along the Amazon River main stem (figure 1). The area of a grid cell is $\sim 765\,km^2$.

Reach	Grid cells	Open-water area (km^2) River	Open-water area (km^2) Lakes	f_w	Upland fraction	ΔT_w	ΔT_f
1	15	570	90	0.06	0.66	48	12
2	28	510	250	0.04	0.66	47	11
3	22	710	350	0.06	0.36	50	9
4	23	840	280	0.06	0.38	69	10
5	13	540	500	0.10	0.35	49	11
6	25	710	1140	0.10	0.44	44	15
7	13	610	580	0.12	0.50	36	22
8	12	860	630	0.15	0.51	46	28
9	23	980	2000	0.17	0.41	48	21
10	22	880	2670	0.21	0.48	42	28
11	15	1330	2470	0.33	0.41	48	35
12	16	910	340	0.10	0.47	59	18
Jurua	60	230	0	0.005	0.65	–	9
Purus	41	730	120	0.03	0.42	58	8
Madeira	40	1010	200	0.04	0.73	62	15

floodplain. At the confluences of major tributaries the grid-cell aggregates for the main stem contained the lowermost courses of the tributaries, including the Içа River from its mouth to 69° W longitude and the Japura and Jutai rivers from their mouths to 2° S and 3° S latitudes, respectively.

3.2. *River stage data*

River stage data were collected by Manaus Harbor Ltd/Portobrás at the Manaus station and at various other stations throughout the study area by DNAEE (the Brazilian Department of Water and Electric Energy), through contracts with the firms CPRM and Hidrologia SA. For each reach, we selected the most appropriate stage station for which data were available for all or most of the SMMR period (figure 1), taking into account the station's proximity as well as the potential influence of major tributaries upstream of the reach. Monthly means were calculated from the daily stage data for comparison with the monthly ΔT_{obs} data.

3.3. *Estimation of flooded area from ΔT_{obs}*

The algorithms for estimation of the fractional area of inundation from the 37 GHz ΔT_{obs} have been described by Sippel *et al.* (1994) and Hamilton *et al.* (1996). A linear mixing model with three end-members incorporates the contributions of water, nonflooded land, and inundated floodplain to the ΔT_{obs}:

$$\Delta T_{obs} = f_w(\Delta T_w) + f_{nf}(\Delta T_{nf}) + f_f(\Delta T_f) \qquad (1)$$

$$1 = f_w + f_{nf} + f_f \qquad (2)$$

where ΔT_{obs} is the ΔT observed by the radiometer, f_w, f_{nf} and f_f are the fractional areas of open water (rivers and permanent floodplain lakes), nonflooded land, and seasonally flooded land, respectively, and ΔT_w, ΔT_{nf} and ΔT_f are the ΔT values for open water, nonflooded land, and seasonally flooded land. As the floodplain becomes inundated, f_f increases with a concomitant decrease in f_{nf}. Simultaneous solution of equations (1) and (2) yields the following equation for the fraction of flooded area (f_f):

$$f_f = \frac{\Delta T_{obs} - f_w(\Delta T_w) - \Delta T_{nf} + f_w(\Delta T_{nf})}{\Delta T_f - \Delta T_{nf}} \tag{3}$$

We measured the fractional area of open water within each grid-cell aggregate (f_w), which includes both the main river channels and permanent floodplain lakes, using 1:250 000 scale planimetric maps produced from SLAR imagery (Sippel *et al.* 1992). Open-water area was measured by digital planimetry of all lakes, rivers and floodplain channels that appear on the maps. The open-water surfaces visible on the SLAR images are assumed to approximate the f_w throughout the inundation period, since most seasonally flooded land is covered by vegetation that remains emergent during inundation, and thus would not produce specular reflection of X-band SLAR energy (Sippel *et al.* 1994). Table 1 shows the open-water areas and the f_w values for each reach.

The three ΔT end-member values needed for equation (3) were determined empirically. We determined a mean ΔT_{nf} value of 4.2 K by averaging all dates for 17 grid cells of upland pixels located along the length of the Amazon River main stem between 55° 30′ and 68° 30′ W longitude (SD=1.0; n=1768 observations). Based on the 1:250 000 Radambrasil maps, these 17 upland grid cells do not contain significant floodplain or open water and they lack streams wider than a single line (i.e., streams of more than *ca* 100 m in width); hence they are presumably not subject to significant seasonal flooding. This mean ΔT_{nf} value was used for all of the study reaches since systematic spatial or seasonal variation in ΔT_{nf} across the region was not apparent.

The two remaining ΔT end-members were determined for each reach individually. We estimated ΔT_w from the ΔT_{obs} at low water, when the seasonally inundated floodplain is dry but water persists in the river channels and in floodplain lake basins. Using the mean ΔT_{obs} for the 24 lowest values in the time series, which typically included 2–4 months in each annual low-water phase, we applied a two end-member mixing model to estimate ΔT_w by simultaneous solution of the two equations:

$$\Delta T_{obs} = (f_w)(\Delta T_w) + (f_{nf})(\Delta T_{nf}) \tag{4}$$

$$1.0 = f_w + f_{nf} \tag{5}$$

where ΔT_{obs} is the mean ΔT observed by the radiometer at low water, f_w is the fractional area of open water (rivers and lakes), f_{nf} is the fractional area of nonflooded land at that time ($=1-f_w$), and ΔT_{nf} is the ΔT value for nonflooded upland that we determined empirically (4.2 K). This method of estimating ΔT_w differs from our previous work (Sippel *et al.* 1994, Hamilton *et al.* 1996) in which we used the theoretical value for ΔT_w of calm water surfaces (60 K). Empirical estimation of ΔT_w for each reach is preferable for this study because some reaches have large expanses of open water, where surface roughness due to wave formation may reduce the mean ΔT_w for the grid-cell aggregate, as has been observed over the ocean (Gloersen *et al.*

1992). Also, if the measurement of f_w from the SLAR maps were an inaccurate representation of open-water area, that error would be compensated by the empirical ΔT_w value. For that reason, the empirical ΔT_w values listed in table 1 should not be considered to have theoretical significance.

We estimated the ΔT_f end-member for each reach from the mean of the four highest ΔT_{obs} values in the time series (choosing a mean to reduce the effects of possible outliers). This mean high-water ΔT_{obs} was assumed to result from complete flooding of the geomorphological floodplain within the reach, which is delineated on the Radambrasil maps and was measured by digital planimetry (Sippel *et al.* 1992, 1994). Thus we used the three end-member model (equation (3)) to estimate ΔT_f from the mean high-water ΔT_{obs}, f_f (the geomorphological floodplain area on Radambrasil maps), the empirically determined values of ΔT_w and ΔT_{nf}, f_w (the open-water area on Radambrasil maps), and f_{nf} ($=1-f_f-f_w$). The unique ΔT_f end member for each reach (table 1) represents the effects of the particular combination of floodplain vegetation and geomorphology on microwave emission from the floodplain during inundation.

The three end-member model (equation (3)) was applied for each date throughout the inundation period to estimate f_f, the fraction of area flooded, from ΔT_{obs}. Total flooded area on a given date is the sum of f_w (open waters) and f_f (seasonally flooded land). When the floodplain was dry, as indicated by a ΔT_{obs} less than the low-water mean, the two end-member model (equations (4) and (5)) and the empirical ΔT_w value were employed to estimate f_w (the area of open water).

3.4. *Sensitivity analysis of the algorithms*

Error in the estimation of flooded area can arise from the five different input terms in equation (3). We performed a sensitivity analysis individually for each term, choosing a typical annual cycle of flooded area for the entire main stem (1982), to demonstrate the sensitivity of the algorithm to errors in the input terms (figure 2). The possible effect of error in ΔT_{obs} and ΔT_{nf} was evaluated by taking the standard deviation of 1768 observations over upland areas (1.0 K) as an estimate of the overall precision for both of these terms. This may overestimate random instrument error or atmospheric variability because it incorporates any temporal variability in emission from the upland areas, although similar variability in the SMMR ΔT_{obs} has been observed over stable regions of the Antarctic ice sheet (Gloersen *et al.* 1992), suggesting that instrument variability is the primary cause. Errors in the ΔT_w, ΔT_f and f_w are indeterminate, so those terms were varied by arbitrary amounts in the sensitivity analysis.

The sensitivity analysis indicates that the estimation of flooded area in the Amazon is particularly sensitive to possible error in the satellite observations (ΔT_{obs}) and to possible bias in our empirical estimates of ΔT_{nf} and ΔT_w. Error in ΔT_{obs} would be particularly significant in reaches with the smallest seasonal range in ΔT_{obs}. Error in ΔT_{nf} and ΔT_w would be most important in reaches with higher fractional areas of upland and open water, respectively (table 1).

4. Results and discussion

4.1. *Inundation patterns in the floodplain of the Amazon River main stem*

The monthly estimates of flooded area in each reach of the Amazon River main stem are plotted together with the data for the appropriate river stage station in figure 3. We define flooded area as the total of inundated floodplain and open-water

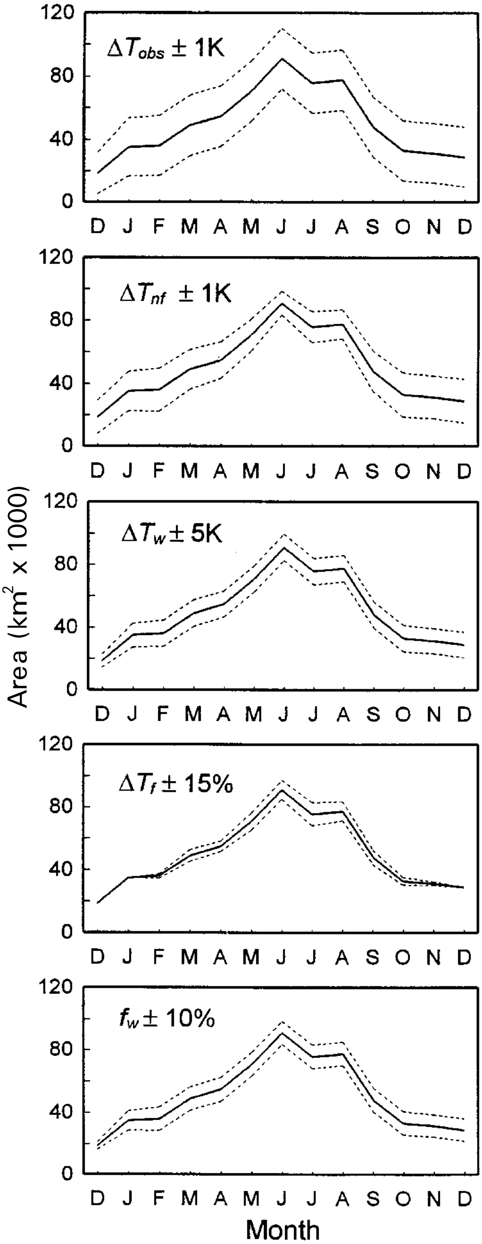

Figure 2. Sensitivity analysis of the algorithm (equation (3)) for estimation of flooded area using data from 1982 as an example. The solid line shows the original flooded area estimates and the dashed lines show the results when a particular input term (as noted on each graph) is varied.

area of lakes and river channels. Most reaches display a unimodal peak in flooded area, and although most of the years in the time series show distinct periods of floodplain inundation and drainage, the maximum and minimum area flooded show notable interannual variability. There are usually more erratic fluctuations on the rising limb than on the falling limb of the flood peak. In a study that encompassed parts of reaches 6 and 7, Sippel *et al.* (1994) attributed some of the variability in ΔT_{obs} on the rising limb of the hydrograph to local rainfall. In theory, heavy rain could decrease ΔT_{obs} by atmospheric scattering or increase ΔT_{obs} by temporary pooling of water on the land surface; the relative importance of these effects in the Amazon region are not known. There are also secondary discharge crests on the rising limb of the river hydrograph that result from the contributions of upriver tributaries with earlier flood peaks; these crests are most pronounced in the upper Amazon and diminish in the downstream direction (figure 3; also Meade *et al.* 1991). However, the timing of these secondary discharge crests does not correspond with all of the observed fluctuations in ΔT_{obs} along the Amazon River main stem, indicating that other causes are also involved in the fluctuations (Sippel *et al.* 1994).

The flooding patterns in reaches 1 and 2 appear erratic compared with the downstream reaches. This could be explained in part by the difficulty of observing the effects of flooding in those reaches, due to the smaller range of variation in ΔT_{obs}. However, more erratic flooding patterns could also be explained by the more variable discharge regimes of the main channel and its major tributaries in the uppermost reaches (Richey *et al.* 1989 a), as well as by the higher rainfall in that region (Salati 1985). More information on flooding patterns in the upper reaches is needed to confirm whether this apparent variability is real.

The time series of total flooded area for the entire Amazon River main stem (i.e., the sum of flooded area in reaches 1–12) is depicted in figure 4, and the monthly means of flooded area are given in table 2. The river stage is for the central Amazon main stem (Manaus station: figure 1). Interannual variation in the maximum and minimum flooded area is clearly visible in the figure. The highest water levels were observed in 1982, corresponding with the greatest area of flooding. In contrast, much less floodplain area was inundated during the floods of 1980, 1983 and 1985. During

Table 2. Monthly and grand means of flooded area ($km^2 \times 10^3$) as estimated from the monthly SMMR observations. The Amazon River includes reaches 1–12 along the main stem. For the Amazon River, means are also provided for the extended 94-year record (see text for explanation). Flooded area includes open waters of river channels and floodplain water bodies as well as the vegetated floodplain. Standard deviations are given in parentheses.

Month	Amazon River 1979–1987	Amazon River 1903–1996	Jurua River 1979–1987	Purus River 1979–1987	Madeira River 1979–1987
Jan	32.5 (6.6)	33.0 (5.2)	4.6 (2.9)	6.0 (2.7)	2.0 (0.8)
Feb	38.2 (4.5)	39.4 (6.2)	6.8 (2.2)	9.8 (2.9)	3.0 (1.0)
Mar	44.6 (10.3)	46.3 (8.0)	8.3 (4.6)	12.4 (2.9)	4.1 (1.4)
Apr	53.4 (11.2)	56.0 (8.7)	10.1 (5.0)	15.1 (2.1)	4.4 (0.5)
May	63.5 (10.3)	66.7 (9.2)	8.6 (2.6)	15.6 (1.8)	5.3 (1.3)
Jun	67.3 (13.9)	72.7 (9.3)	8.5 (2.7)	15.6 (4.1)	5.3 (1.6)
Jul	63.9 (11.1)	70.1 (9.8)	6.9 (3.9)	13.0 (4.9)	4.5 (1.4)
Aug	56.6 (15.8)	57.7 (10.9)	5.9 (4.1)	9.7 (5.1)	3.7 (1.7)
Sep	37.5 (13.8)	38.9 (10.0)	2.1 (2.4)	4.3 (3.8)	1.8 (0.9)
Oct	28.1 (9.8)	27.0 (5.8)	0.8 (0.8)	2.1 (2.2)	1.3 (0.7)
Nov	26.7 (10.8)	25.6 (4.0)	2.7 (2.4)	2.1 (2.0)	1.4 (0.9)
Dec	30.2 (10.7)	28.1 (4.2)	3.7 (2.4)	4.2 (3.1)	1.8 (1.0)
All dates	45.9 (17.5)	46.8 (18.4)	6.0 (4.2)	10.0 (6.2)	3.3 (1.8)

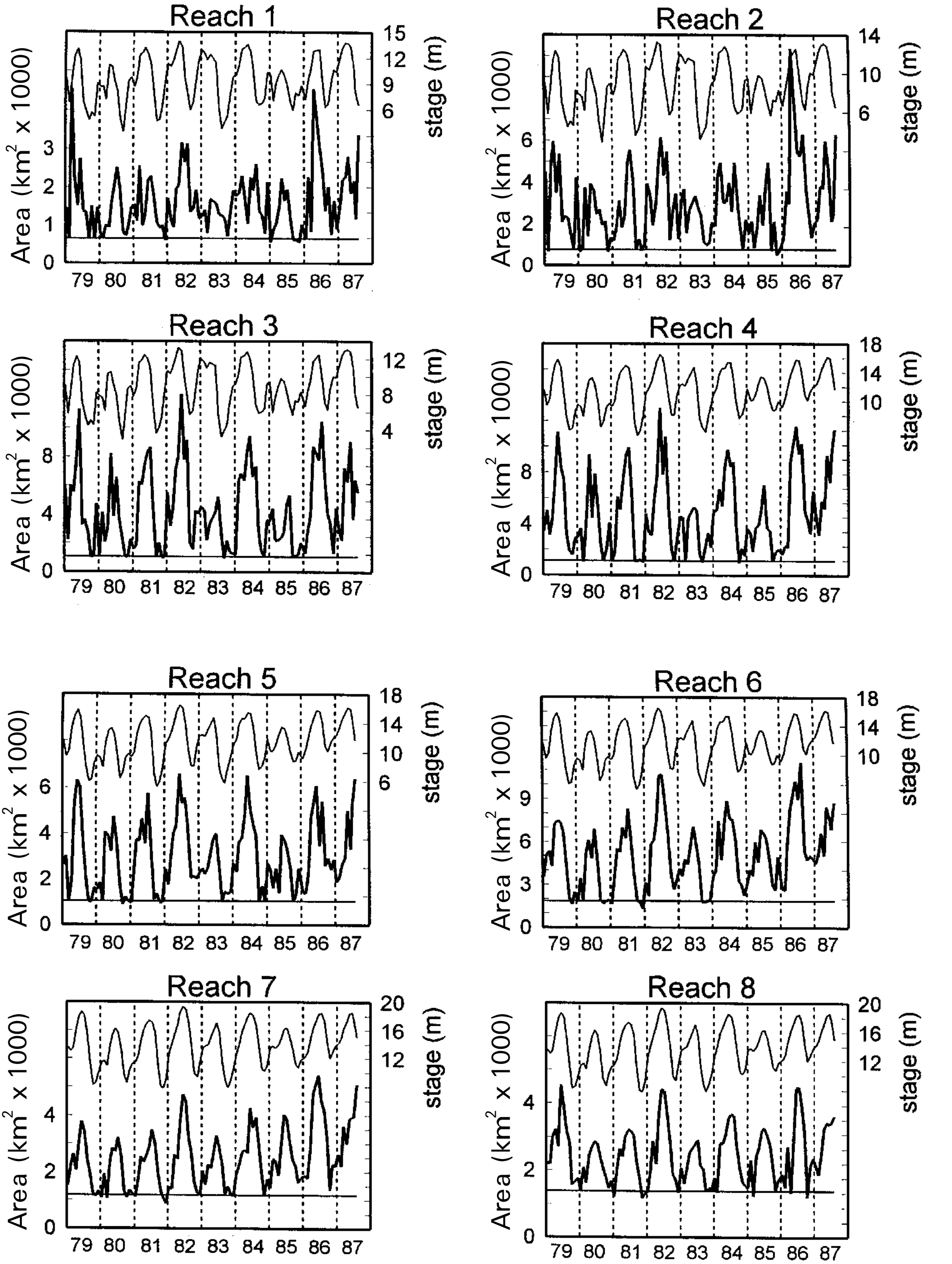

Figure 3. Monthly estimates of the total flooded area (inundated floodplain plus rivers and lakes) for each reach of the Amazon River main stem. Flooded area is depicted by bold lines, with the river stage plotted above for comparison (stage stations corresponding to each reach are identified in table 3). The horizontal lines show the open-water areas from table 1. When the flooded area is at or below the horizontal line, no floodplain is inundated and only open water is present.

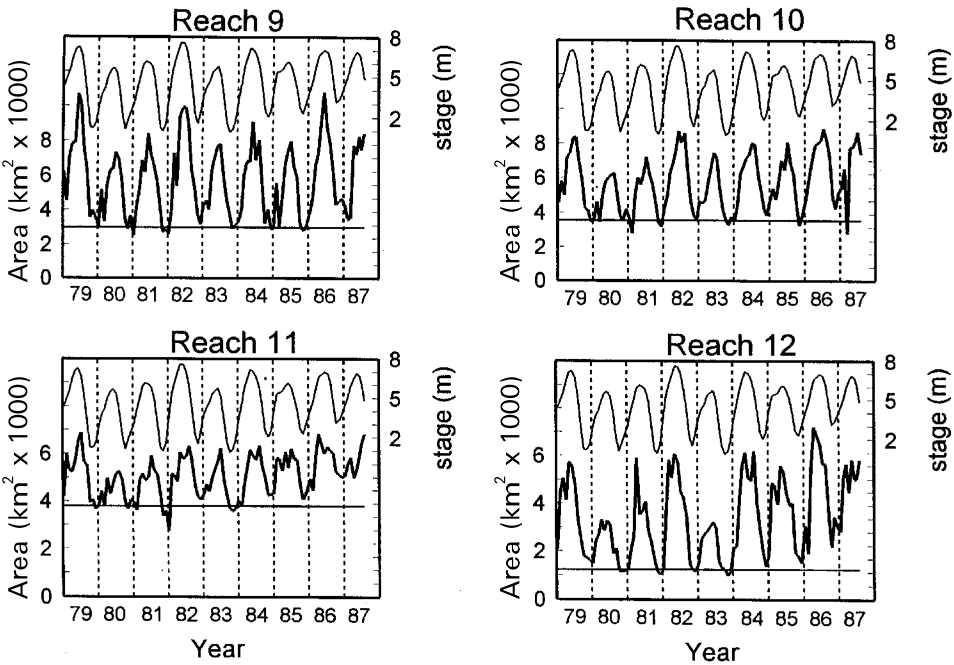

Figure 3. (*continued*).

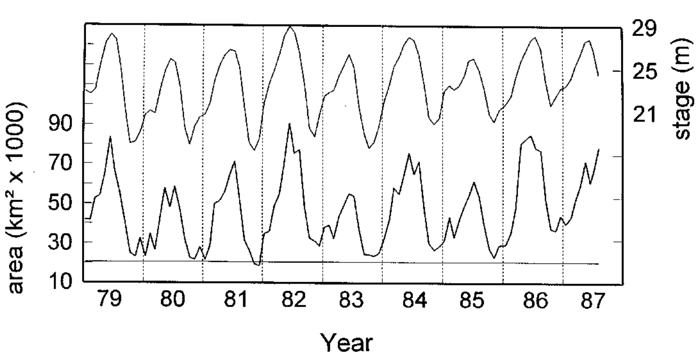

Figure 4. Monthly estimates of total flooded area (inundated floodplain plus rivers and lakes) for the entire Amazon River main stem (sum of reaches 1–12), plotted together with the river stage at Manaus. Flooded area is depicted by the lower line, with stage plotted above. The horizontal line shows the open-water area from table 1. When the flooded area is at or below the horizontal line, no floodplain is inundated and only open water is present.

the 9 years of the SMMR observations, inundation of the main-stem floodplain tended to peak between May and July, with minimal inundation between October and December.

4.2. *Inundation patterns in the tributary floodplains*

The three tributaries analysed in this study show distinct seasonal patterns of floodplain inundation (figure 5), which reflect their distinct discharge regimes. The changes in flooded area along both the Madeira and Purus rivers are relatively

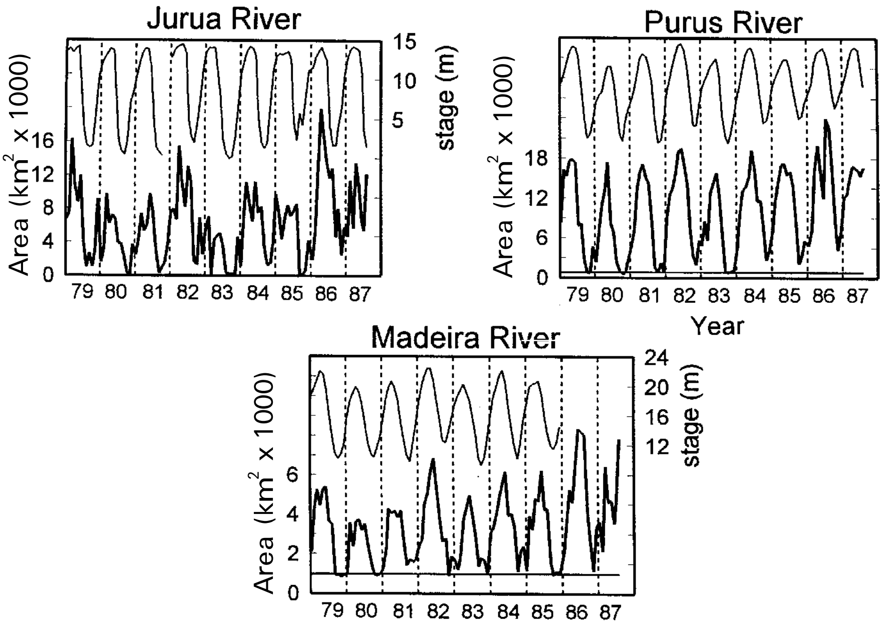

Figure 5. Monthly estimates of total flooded area (inundated floodplain plus rivers and lakes) for the Jurua, Purus and Madeira rivers, three major tributaries of the Amazon River. Flooded area is depicted as bold lines, with the available river stage plotted above for comparison (stage stations are identified in table 3). The horizontal lines show the open-water areas from table 1 (open-water area is insignificant in the Jurua River). When the flooded area is at or below the horizontal line, no floodplain is inundated and only open water is present.

gradual and inundation tends to peak in both floodplains in May to June (table 2). Inundation in the Jurua River floodplain appears more erratic but tends to peak earlier, usually between March and June. The relatively erratic pattern of flooded area along the Jurua River may be caused at least partly by the small variation in ΔT_{obs}, which renders background variability more significant. Unlike the other rivers analysed in this study, however, the stage in the Jurua River displays truncation at high water, implying that at peak discharges the excess water is largely absorbed by the floodplain without producing a concomitant increase in water level. Thus the area flooded along the Jurua River could fluctuate substantially as discharge varies during the high-water period, even though the river stage changes little.

4.3. *Relation between ΔT_{obs} and river stage*

River level (stage) observations provide the best available proxy for temporal variations in flooded area on the floodplains that fringe the major rivers of the Amazon system and therefore serve to corroborate the passive microwave observations. Studies along the Amazon River main stem have shown that although water on the floodplains may originate from local runoff as well as riverine overflow, the river largely controls water levels and thus flooded area on the adjacent floodplain (Forsberg *et al.* 1988, Lesack and Melack 1995). Comparison of time series of river stage with the corresponding time series of ΔT_{obs} therefore helps to verify that seasonal changes in ΔT_{obs} reflect changes in flooded area rather than some other seasonal phenomenon. The closest river stage stations are outside of the main-stem reaches in some cases (figure 1), but this would introduce a time delay of no more than 1–2 weeks. Thus the correlations between river stage and ΔT_{obs} provide an indication of how well the changes in ΔT_{obs} correspond with changes in flooded area in the various study reaches.

Pearson product-moment correlations between ΔT_{obs} and the appropriate river stage for each reach are summarized in table 3, which includes contemporaneous correlations as well as time lags of up to 3 months each way (Systat 1992). Contemporaneous correlations range from *ca* 0.4 in reaches 1 and 2 to *ca* 0.9 in reach 12 and in the Purus River floodplain. In many reaches the correlation improved considerably with a time lag of -1 month (i.e., changes in ΔT_{obs} tend to occur 1 month later than changes in river stage). Time lags of >3 months did not improve the correlations. In large floodplains, a negative lag on the order of 1 month may be explained by the delayed filling and drainage of the floodplain relative to the rise and fall of the river, as illustrated by a comparison of river and floodplain stage for the Orinoco River in Venezuela (Hamilton and Lewis 1990). Flooding by smaller tributaries and local runoff would typically precede the flood wave along the Amazon River main stem (Lesack and Melack 1995), and thus would not explain the apparent time delay of flooding relative to river stage.

The small seasonal variation in the ΔT_{obs} over upland areas adjacent to the floodplain compared with the variation over floodplain areas, as shown by the example in figure 6, provides further support for the conclusion that the seasonal variation in ΔT_{obs} over South American floodplains is produced by flooding rather than by atmospheric variability (Hamilton *et al.* 1996). Even though seasonal

Table 3. Pearson correlations between ΔT_{obs} and the appropriate river stage for each reach, including the contemporaneous correlation (lag 0) as well as correlations with time lags of up to 3 months each way. In each case, the best correlation (marked in bold) is significant at $p<0.001$. A maximum correlation at a lag of -1 indicates that changes in ΔT_{obs} tend to occur 1 month later than changes in river stage. Codes for river stage sites are identified in figure 1. The 104 monthly observations were included in each of the correlations.

Reach	Stage site	Correlation coefficients (time lags in months)						
		−3	−2	−1	0	+1	+2	+3
1	SPO	0.30	**0.41**	0.38	0.38	0.15	−0.08	−0.22
2	SAI	0.32	0.47	**0.48**	0.44	0.21	−0.03	−0.25
3	SAI	0.35	0.61	**0.71**	0.61	0.23	−0.09	−0.33
4	ITA	0.20	0.50	0.77	**0.81**	0.53	0.12	−0.22
5	ITA	0.28	0.58	**0.80**	0.78	0.47	0.06	−0.27
6	ITA	0.35	0.67	**0.86**	0.82	0.52	0.13	−0.19
7	MNC	0.26	0.59	0.82	**0.84**	0.60	0.23	−0.14
8	MNC	0.34	0.65	**0.83**	0.81	0.51	0.11	−0.28
9	OBI	0.45	0.74	**0.86**	0.78	0.45	0.03	−0.38
10	OBI	0.46	0.74	**0.89**	0.80	0.49	0.07	−0.31
11	OBI	0.49	0.74	**0.86**	0.73	0.41	0.04	−0.27
12	OBI	0.20	0.56	0.82	**0.88**	0.72	0.43	0.08
Jurua	JUR	0.42	**0.62**	0.61	0.45	0.22	−0.09	−0.36
Purus	PUR	0.18	0.55	0.83	**0.89**	0.73	0.41	0.03
Madeira	MAD	0.52	0.79	**0.88**	0.74	0.41	0.01	−0.37

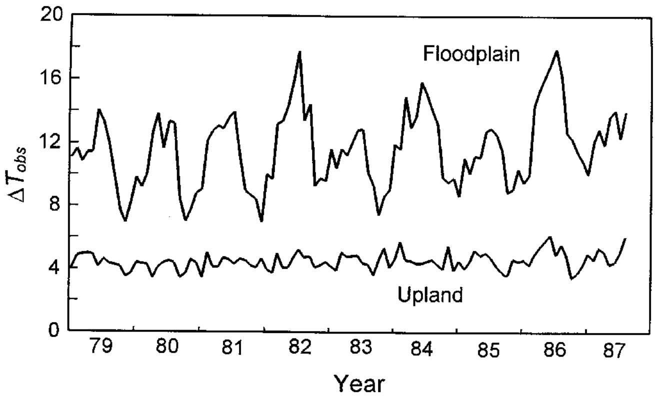

Figure 6. Comparison of the ΔT_{obs} over the floodplain of the Amazon River main stem (mean for two grid cells in reach 6) with the ΔT_{obs} over nearby upland areas (mean for five grid cells adjacent to reach 6). These data were selected as an example to show the effect of seasonal inundation on ΔT_{obs}.

flooding drives the variation, the absolute value of the ΔT_{obs} may still be modulated by atmospheric effects (Kerr and Njoku 1993). Modulation of the ΔT_{obs} by atmospheric moisture would be greatest during the wet season, which generally peaks in January to April, whereas the river stage generally peaks in May to July along the Amazon River main stem. Seasonal changes in atmospheric effects on ΔT_{obs} could therefore produce an apparent time delay in ΔT_{obs} relative to stage if the modulation occurred more during the rising limb of the flood hydrograph. Regardless of whether atmospheric variability may modulate the ΔT_{obs} and thereby cause the apparent time delays observed in many of the reaches, it is evident that the observed variation in ΔT_{obs} over the floodplain is driven largely by riverine flooding and thus can be used as an indicator of the extent of flooding.

The reaches showing the poorest correlations between river stage and ΔT_{obs} are the main-stem reaches 1 and 2, and the Jurua River floodplain (table 3). These reaches also have relatively small seasonal ranges in ΔT_{obs} (figure 7). Excluding the uppermost and lowermost 10% of the values, the range in ΔT_{obs} in these reaches was <1.5 K, which is comparable to the standard deviation observed for upland pixels (1.0 K). In these reaches it is thus difficult to discern the effects of seasonal inundation and drainage of the floodplain on the ΔT_{obs}, which may explain the relatively poor correlations. The attenuated stage of the Jurua River reduces the correlation between stage and ΔT_{obs}, and by causing the stage data to be non-normally distributed, it violates an underlying assumption of parametric correlation analysis used in table 3 (the Jurua is the only case where the frequency distribution of the stage data is markedly non-normal). The range in ΔT_{obs} over the Purus and the Madeira floodplains is also <2 K, but these reaches show better correlations between stage and ΔT_{obs}. In contrast, the ΔT_{obs} in reaches 4–12 of the Amazon River main stem spanned 2–7 K between the 10th and 90th percentiles, which makes the floodplain signal more readily discernible over background variability. We also investigated whether the correlation between ΔT_{obs} and stage might be related to the number of grid cells in the aggregate (expecting a positive relationship if geolocation error is important) or the fractional open-water area (expecting a negative

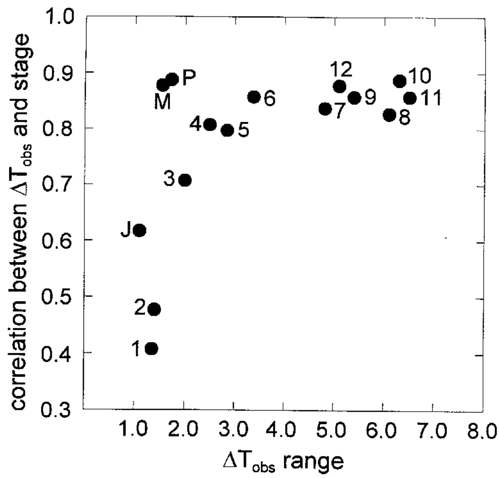

Figure 7. The Pearson correlation coefficient between ΔT_{obs} and river stage (best correlations from table 3) plotted against the range (10th to 90th percentiles) of the ΔT_{obs} in each reach. Labels identify the 12 reaches of the Amazon River main stem and the three tributary reaches (J = Jurua, P = Purus, M = Madeira).

relation if the open-water ΔT_w is highly variable in time). However, scatterplots did not reveal such relationships.

4.4. *Reconstruction of a 94-year time series of flooded area*

The correlation between river stage and total flooded area (figure 8) allows us to extend the record of flooded area beyond the 9-year SMMR time series. The longest stage record for the region is from Manaus, located on the Negro River close to the Amazon River main stem (figure 1), where data have been collected since 1903. The stage at Manaus is controlled by backflooding from the Amazon River main stem because the water surface slope between the stage station and the main stem is very slight. We regressed our monthly estimates of total flooded area (in km^2) for the

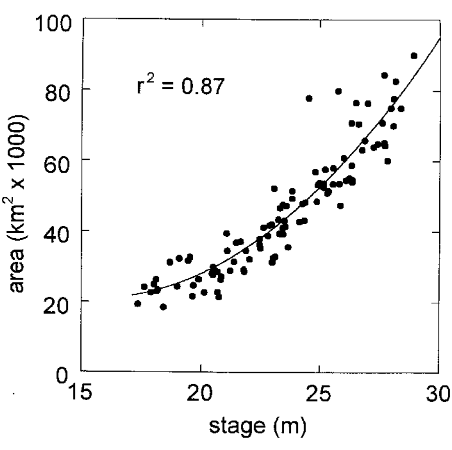

Figure 8. The relationship between the total flooded area along the Amazon River main stem (data from figure 4) and the monthly means of river stage at Manaus. The regression line (equation (6)) is also plotted.

main-stem Amazon floodplain from January 1979 to August 1987 on the mean monthly stage at Manaus (in m) to yield the following predictive equation (plotted in figure 8), which was employed to reconstruct the flooded area at monthly intervals for 1903–1996:

$$Y = 104\ 744 - 10\ 851X + 351X^2 \ (r^2 = 0.87,\ p \leqslant 0.001,\ n = 102) \tag{6}$$

The standard error of the estimate is 6400 km^2. The total flooded area is for reaches 1–12 of the Amazon River main stem and does not include floodplains extending up the tributaries. The range in stage during 1903–1996 was similar to that observed during the January 1979 to August 1987 period from which the model was derived, except for occasional very low stages during dry periods. We lack SMMR observations of flooded area at stages <17.34 m, so we used a fixed value of 22 100 km^2 for those dates, which is the area predicted by equation (6) for a stage of 17.34 m.

The reconstructed long-term record of flooded area for the Amazon River main stem is shown in figure 9. Nearly every year in the record displayed a distinct unimodal rise and fall in flooded area. The only exception was 1926, a year in which observers recorded a protracted drought and widespread fires (recounted by Sternberg 1987). In the majority of years, the vegetated floodplain dried completely or nearly so during the dry season, but for only a few months. The mean flooded area for the 94-year record, which includes floodplain plus river and lake area, is 46 800 km^2. Of this, ~20 700 km^2 is open water, including both river channels and floodplain waters (table 1). Thus the portion of this mean flooded area that is covered by vegetated floodplain is ~26 100 km^2, or 37% of the 71 200 km^2 of vegetated floodplain within reaches 1–12 that is delineated on the Radambrasil maps. The seasonal cycle in the monthly means of flooded area for the 94-year record resembles that for the 9-year SMMR observation period, and therefore the SMMR period is representative of the typical flooding patterns (table 2).

Richey *et al.* (1989 b) analysed the long-term stage record for the Amazon River and concluded that the predominant interannual variability occurs on the scale of 2–3 years, and that this variability is coupled to the El Niño–Southern Oscillation phenomenon (the occasional changes in surface temperature patterns in the tropical Pacific Ocean that produce worldwide changes in atmospheric circulation and weather). Since stage is related to flooding (figure 8), those conclusions regarding the effects of El Niño on the Amazon River stage record apply to floodplain inundation as well.

The long-term inundation record for the Amazon River main stem can be compared to a similar record that we have reconstructed for the Pantanal wetland, a major floodplain complex located south of the Amazon Basin (Hamilton *et al.* 1996). Inundation of the Amazon River floodplain is much less variable among years than is inundation in the Pantanal, which has experienced two multiyear droughts with little or no floodplain inundation during the past 95 years. The greater predictability of the flood pulse in the Amazon floodplain is not surprising because the flooding is largely driven by the river, which drains a much larger basin (6×10^6 km^2 compared with 5×10^5 km^2 for the Paraguay River in the Pantanal). The seasonal and interannual variability of runoff is also more predictable in the Amazon Basin because of the higher overall rainfall and its more equitable seasonal distribution in much of the basin, as well as the ~6-month offset in the peak rainfall months on either side of the equator that divides the basin (Salati 1985).

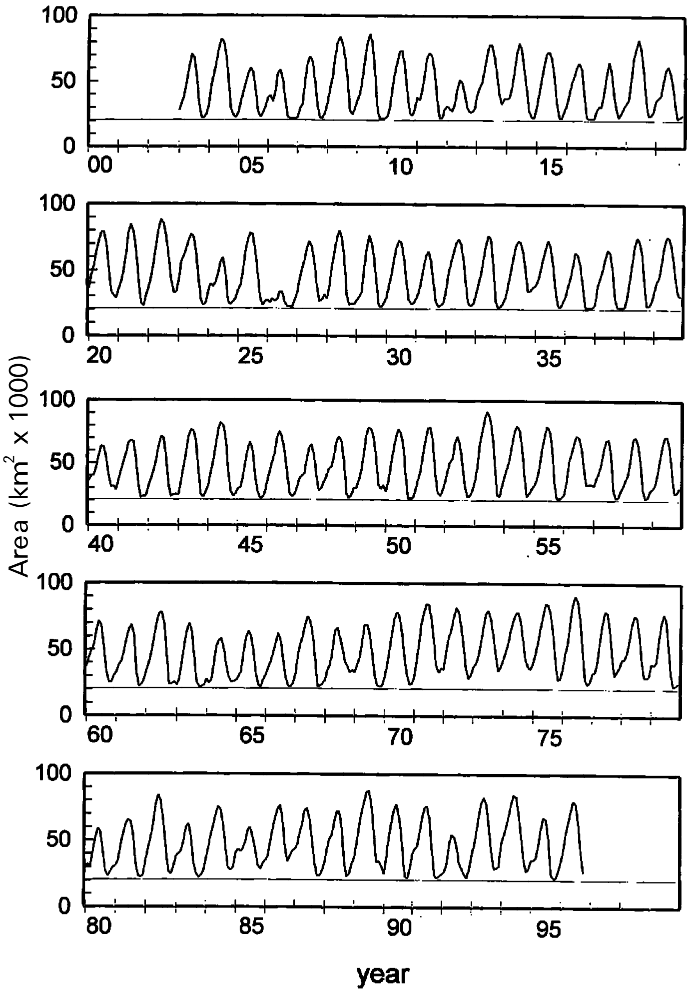

Figure 9. A 94-year reconstruction of flooded area (inundated floodplain plus rivers and lakes) from the river stage record, based on the relationship in figure 8. The horizontal line shows the total open-water area (river channels plus permanent floodplain lakes). The long-term mean of the flooded area along the Amazon River main stem is 46 830 km^2.

5. Conclusions

This study has successfully employed the SMMR 37 GHz polarization difference to produce a 9-year record of temporal changes in inundation of the floodplains of the Amazon River and its major tributaries. In addition to providing information on the seasonal and interannual variation in inundation for each individual reach, we have formulated a predictive relationship between the Amazon River stage at Manaus and the total area inundated in the fringing floodplain, allowing extrapolation of the inundation record over the 94 years of stage records. These data on the spatial and temporal variability of floodplain inundation—as well as the capability to predict inundation area from river stage—are of fundamental value for hydrological and biogeochemical models of the Amazon River system, ecological studies of the floodplain biota, analyses of the environmental impact of river impoundment and other channel alterations, and socioeconomic studies that require information on the hazards of flooding to humans and human activities on the floodplains.

The usefulness of the SMMR observations for studies of inundation in large riverine floodplains indicates that the similar SSM/I observations made by satellites since the SMMR period are also potentially valuable for this purpose. Future research should seek to extend the passive microwave inundation record for large floodplains such as the Amazon to the present using the SSM/I observations. If the processed SSM/I data could be made available in real time, the potential for flood prediction based on satellite observations of upriver flooding would be enhanced, helping to compensate for the often sparse networks of river stage monitoring stations in remote regions (Vörösmarty *et al*. 1996).

Acknowledgments

This research was supported by the US National Aeronautics and Space Administration through grants NAGW-4352, NAGW-2652 and NAGW-2724. We are grateful to NASA for making the SMMR data set available. J.E. Richey, L.A.K. Mertes, B.R. Forsberg, M. Gastil, E. Njoku and S. Saatchi provided information and assistance. The W.K. Kellogg Biological Station of Michigan State University furnished logistical support. We particularly wish to acknowledge the Brazilian agencies and citizens living along the rivers who have worked diligently for decades to record river levels at stations throughout the Amazon, thereby generating critical information to verify the accuracy of the results we obtained from satellite observations.

References

Bartlett, K. B., and Harriss, R. C., 1993, Review and assessment of methane emissions from wetlands. *Chemosphere*, **26,** 261–320.

Choudhury, B. J., 1989, Monitoring global land surface using Nimbus-7 37 GHz data, theory and examples. *International Journal of Remote Sensing*, **10,** 1579–1605.

Choudhury, B. J., 1991, Passive microwave remote sensing contribution to hydrological variables. *Surveys in Geophysics*, **12,** 63–84.

Choudhury, B. J., Major, E. R., Smith, E. A., and Becker, F., 1992, Atmospheric effects on SMMR and SSM/I 37 GHz polarization difference over the Sahel. *International Journal of Remote Sensing*, **13,** 3443–3463.

Devol, A. H., Richey, J. E., Forsberg, B. R., and Martinelli, L. A., 1990, Seasonal dynamics in methane emissions from the Amazon river floodplain to the troposphere. *Journal of Geophysical Research*, **95,** 16417–16426.

Forsberg, B. R., Devol, A. H., Richey, J. E., Martinelli, L. A., and Dos Santos, H., 1988, Factors controlling nutrient concentrations in Amazon floodplain lakes. *Limnology and Oceanography*, **33,** 41–56.

Frechione, J., Posey, D. A., and Silva, L. F., 1989, The perception of ecological zones and natural resources in the Brazilian Amazon: an ethnoecology of Lake Coari. *Advances in Economic Botany*, **7,** 260–282.

Fu, C. C., Han, D., Kim, S. T., and Gloersen, P., 1988, User's guide for the Nimbus 7 Scanning Multichannel Microwave Radiometer (SMMR) CELL-ALL tape. NASA Reference Publication, 1210, US National Aeronautics and Space Administration, Washington, DC, USA.

Giddings, L., and Choudhury, B. J., 1989, Observation of hydrological features with Nimbus-7 37 GHz data, applied to South America. *International Journal of Remote Sensing*, **10,** 1673–1686.

Gloersen, P., Cavalieri, D. J., Chang, A. T. C., Wilheit, T. T., Campbell, W. J., Johannessen, O. M., Katsaros, K. B., Kunzi, K. F., Ross, C. B., Staelin, D., Windsor, E. P. L., Barath, F. T., Gudmandsen, P., Langham, E., and Ramseier, R. O., 1984, A summary of results from the first Nimbus 7 SMMR observations. *Journal of Geophysical Research*, **89,** 5335–5344.

Gloersen, P., Campbell, W. J., Cavalieri, D. J., Comiso, J. C., Parkinson, C. L., and Zwally, H. J., 1992, Arctic and Antarctic Sea Ice, 1978–1987: Satellite Passive-Microwave Observations and Analysis. NASA SP-511, US National Aeronautics and Space Administration, Washington, DC, USA.

Hamilton, S. K., and Lewis, W. M. Jr. 1990, Physical characteristics of the fringing floodplain of the Orinoco River, Venezuela. *Interciencia*, **15,** 491–500.

Hamilton, S. K., Sippel, S. J., and Melack, J. M., 1996, Inundation patterns in the Pantanal wetland of South America determined from passive microwave remote sensing. *Archiv für Hydrobiologie*, **137**, 1–23.

Hamilton, S. K., Sippel, S. J., Calheiros, D. F., and Melack, J. M., 1997, An anoxic event and other biogeochemical effects of the Pantanal wetland on the Paraguay River. *Limnology and Oceanography*, **42,** 257–272.

Hess, L. L., Melack, J. M., Filoso, S., and Wang, Y., 1995, Delineation of inundated area and vegetation along the Amazon floodplain with the SIR-C synthetic aperture radar. *IEEE Transactions on Geoscience and Remote Sensing*, **33,** 896–904.

Hollinger, J. P., Pierce, J. L., and Poe, G. A., 1990, SSM/I instrument evaluation. *IEEE Transactions on Geoscience and Remote Sensing*, **28,** 781–790.

Junk, W. J., 1997, The central Amazon floodplain: ecology of a pulsing system. *Ecological Studies*, Volume 126 (New York: Springer), 525 pp.

Kerr, Y. H., and Njoku, E. G., 1993, On the use of passive microwaves at 37 GHz in remote sensing of vegetation. *International Journal of Remote Sensing*, **14,** 1931–1943.

Lesack, L. F. W., and Melack, J. M., 1995, Flooding hydrology and mixture dynamics of lake water derived from multiple sources in an Amazon floodplain lake. *Water Resources Research*, **31,** 329–345.

Lewis, W. M. Jr, and Saunders, J. F. III, 1989, Concentration and transport of dissolved and suspended substances in the Orinoco River. *Biogeochemistry*, **7,** 203–240.

Ligon, F. K., Dietrich, W. E., and Trush, W. J., 1995, Downstream ecological effects of dams. *BioScience*, **45,** 183–192.

Meade, R. H., Rayol, J. M., Da Conceicão, S., and Natividade, J. R. G., 1991, Backwater effects in the Amazon River Basin of Brazil. *Environmental Geology Water Sciences*, **18,** 105–114.

Mertes, L. A. K., Dunne, T., and Martinelli, L. A., 1996, Channel-floodplain geomorphology along the Solimões–Amazon River, Brazil. *Geological Society of America Bulletin*, **108,** 1089–1107.

Petts, G. E., 1990, Regulation of large rivers: problems and possibilities for environmentally-sound river development in South America. *Interciencia*, **15,** 388–395.

Richey, J. E., Mertes, L. A. K., Dunne, T., Victoria, R. L., Forsberg, B. R. Tancredi, C., and Oliveira, E., 1989 a, Sources and routing of the Amazon River flood wave. *Global Biogeochemical Cycles*, **3,** 191–204.

Richey, J. E., Nobre, C., and Deser, C., 1989 b, Amazon River discharge and climate variability: 1903 to 1985. *Science*, **246,** 101–103.

Richey, J. E., Victoria, R. L., Salati, E., and Forsberg, B. R., 1991, The biogeochemistry of a major river system: the Amazon case study. In *Biogeochemistry of Major World Rivers*, edited by E. T. Degens, S. Kempe and J. E. Richey (New York: John Wiley), pp. 57–74.

Salati, E., 1985, The limnology and hydrology of Amazonia. In *Amazonia*, edited by G. T. Prance and T. E. Lovejoy (Oxford: Pergamon), pp. 18–48.

Sioli, H., 1966, General features of the delta of the Amazon. *Proceedings of the Dacca Symposium, Humid Tropical Zone Deltas and their Implications* (Paris: United Nations Educational, Scientific, and Cultural Organization), pp. 381–390.

Sioli, H., 1984, The Amazon and its main affluents: hydrography, morphology of the river courses, and river types. In *The Amazon: Limnology and Landscape Ecology of a Mighty Tropical River and its Basin*, edited by H. Sioli (Dordrecht: W. Junk), pp. 127–166.

Sippel, S. J., Hamilton, S. K., and Melack, J. M., 1992, Inundation area and morphometry of lakes on the Amazon River floodplain, Brazil. *Archiv für Hydrobiologie*, **123,** 385–400.

Sippel, S. J., Hamilton, S. K., and Melack, J. M., 1994, Determination of inundation area in the Amazon River floodplain using the SMMR 37 GHz polarization difference. *Remote Sensing of Environment*, **48,** 70–76.

SYSTAT 1992, *Systat for Windows: Statistics, Version 5 Edition* (Evanston, Illinois: Systat), 750 pp.

Sternberg, H. O. R., 1987, Aggravation of floods in the Amazon River as a consequence of deforestation? *Geografiska Annaler*, **69A,** 201–219.

Vörösmarty, C. J., Moore, B., III, Grace, A. L., and Gildea, M. P., 1989, Continental scale models of water balance and fluvial transport: an application to South America. *Global Biogeochemical Cycles*, **3,** 241–265.

Vörösmarty, C. J., Willmott, C. J., Choudhury, B. J., Schloss, A. L., Stearns, T. K., Robeson, S. M., and Dorman, T. J., 1996, Analyzing the discharge regime of a large tropical river through remote sensing, ground-based climatic data, and modeling. *Water Resources Research*, **32,** 3137–3150.